Research in Astron. Astrophys. **2012** Vol. **12** No. **11**, 1535–1548
http://www.raa-journal.org *http://www.iop.org/journals/raa*

Research in Astronomy and Astrophysics

Analysis of the CME-driven shock from the SEP event that occurred on 2006 December 14 *

Xin Wang[1,2] and Yi-Hua Yan[1]

[1] Key Laboratory of Solar Activities, National Astronomical Observatories, Chinese Academy of Sciences, Beijing 100012, China; *wangxin@nao.cas.cn; yyh@nao.cas.cn*
[2] State Key Laboratory of Space Weather, Chinese Academy of Sciences, Beijing 100080, China

Received 2012 April 12; accepted 2012 May 7

Abstract In a solar flare or coronal mass ejection (CME), observations of the subsequent interplanetary shock provide us with strong evidence of particle acceleration to energies of multiple MeV, even up to GeV. Diffusive shock acceleration is an efficient mechanism for particle acceleration. For investigating the shock structure, the energy injection and energy spectrum of a CME-driven shock, we perform a dynamical Monte Carlo simulation of the CME-driven shock that occurred on 2006 December 14 using an anisotropic scattering law. The simulated results of the shock's fine structure, particle injection, and energy spectrum are presented. We find that our simulation results give a good fit to the observations from multiple spacecraft.

Key words: acceleration of particles — shock waves — Sun: coronal mass ejections (CMEs) — solar wind — methods: numerical

1 INTRODUCTION

It is widely accepted that there are two classes of solar energetic particle (SEP) events, although recent observations indicate that the actual processes may be much more complicated (Pick & Vilmer 2008). The first class is normal impulsive SEP events, which are connected with a large solar flare (Miller 1997). The second class is gradual SEP events, which are responsible for diffusive shock acceleration (DSA) associated with fast coronal mass ejections (CMEs) (Cane et al. 1991; Yan et al. 2006). In a region where solar magnetic connection occurs, CMEs and flares are two manifestations of the same magnetic energy release process (Wang et al. 1996; Zhang et al. 2001, 2007). Both CMEs and flares result in particle accelerations that constitute an SEP event. However, which manifestation dominates the particle injection is still not clear (Li et al. 2009; Le et al. 2012; Qin & Shalchi 2009). Some numerical models suggest that particle accelerations from a combination of both flares and CME-driven shocks provide much better fits to the in-situ observations. Since the process of particle injection is connected with complicated nonlinear effects involved with particle acceleration and also there exist different mechanisms of injection in both processes, we propose a numerical model only involving a shock to calculate the particle injection in the CME-driven shock. We expect that this model would be helpful for understanding the particle injection problem in SEP events.

DSA theory was first introduced in the late 1970s (Krymskii 1977; Axford et al. 1977; Bell 1978; Blandford & Ostriker 1978). In the past several decades, observational data from many spacecraft

* Supported by the National Natural Science Foundation of China.

have increased and investigated the nonlinear diffusive shock acceleration (NLDSA) mechanism, which is the most efficient accelerator in many astrophysical and space environments (Bednarz & Ostrowski 1999; Malkov & O'C Drury 2001; Bykov et al. 2009; Bykov & Treumann 2011; Lu et al. 2006; Zhang et al. 2006). With the development of technology used in observational equipment, especially for spacecraft working in deep space, there have been many models that describe the various nonlinear interactions with the DSA. Several main approaches for studying the NLDSA include: the two-fluid model (Drury & Voelk 1981; Drury et al. 1982); the numerical model (Berezhko & Völk 2000; Kang & Jones 2007; Zirakashvili 2007; Verkhoglyadova et al. 2010); the stationary or dynamical Monte Carlo model (Ellison & Eichler 1984; Knerr et al. 1996; Vladimirov et al. 2006); and the semi-analytical model (Malkov et al. 2000; Caprioli et al. 2010). Among these approaches, the Monte Carlo method addresses the nonlinear effects of DSA by assuming that the entire population of particles undergoes a random walk under a certain scattering law (Ellison et al. 1990; Knerr et al. 1996; Wang & Yan 2011a).

There are three important non-linear processes of DSA theory including particle injection, particle confinement, and shock robustness (Malkov & O'C Drury 2001; Hu 2009). Owing to the fact that walking processes of the particles can be controlled self-consistently in the Monte Carlo method, the Monte Carlo method has an advantage for simulating particle injection. We have already studied the energy translation processes of an Earth-bow shock using the dynamical Monte Carlo method with multiple anisotropic scattering angular distributions (Wang & Yan 2011b). We find that the acceleration efficiency increases as the dispersion of the scattering angular distribution increases from an anisotropic case to an isotropic case. Here, we will further investigate this important particle injection problem in the CME-driven shock using the dynamical Monte Carlo method. There exist a few different properties between the Earth-bow shock and the CME-driven shock: Firstly, the Earth-bow shock has a stationary downstream bulk flow but the CME-driven shock has a dynamical downstream bulk flow; Secondly, the CME-driven shock front has an opposite direction compared to the evolution of Earth's bow shock; Thirdly, the CME-driven shock has the structure of an extended plane shock front near the Earth, but the bow shock front from Earth has a stationary geometry. We predict those differences would produce different non-linear properties including evolution of the shock's fine structure, energy injection rate and even spectral shape of the energy. This paper will focus on understanding some of the non-linear properties of the planetary CME-driven shock. The shock event that occurred on 2006 Dec 14 was fortuitous as it provides us an opportunity for applying code from the dynamical Monte Carlo package, which was developed on the Matlab platform (Wang & Yan 2011a).

This paper is structured as follows: in Section 2, we present the specific observations for the 2006 December 14 CME-driven shock event. The detailed description of the method is given in Section 3. We present the simulated results and discussions in Section 4. Finally, Section 5 presents the summary and some conclusions.

2 OBSERVATIONS

An unusual group of CME-driven shock events that occurred during solar cycle 23 was observed in December 2006 at the solar active region 10930. Halo CMEs were observed by the LASCO coronagraphs in association with the events of 13 and 14 December, with speeds of 1774 km s^{-1} and 1042 km s^{-1}, respectively. Because the 14 December solar event was better magnetically connected to the Earth, it provided the best opportunity for testing the nonlinear effect and efficiency of the DSA mechanism. As shown in Figure 1, an overview of key parameter observations from the Proton Monitor (PM) instruments on Wind/SWE for the CME shock event of 2006 December 14 is given in detail. This event originated on the western hemisphere of the Sun. It showed an abrupt fluctuation in intensity of proton density and thermal speed of the solar wind during the decay of the 13 December solar event. The initial particle increase following the 14 December solar event was seen in the

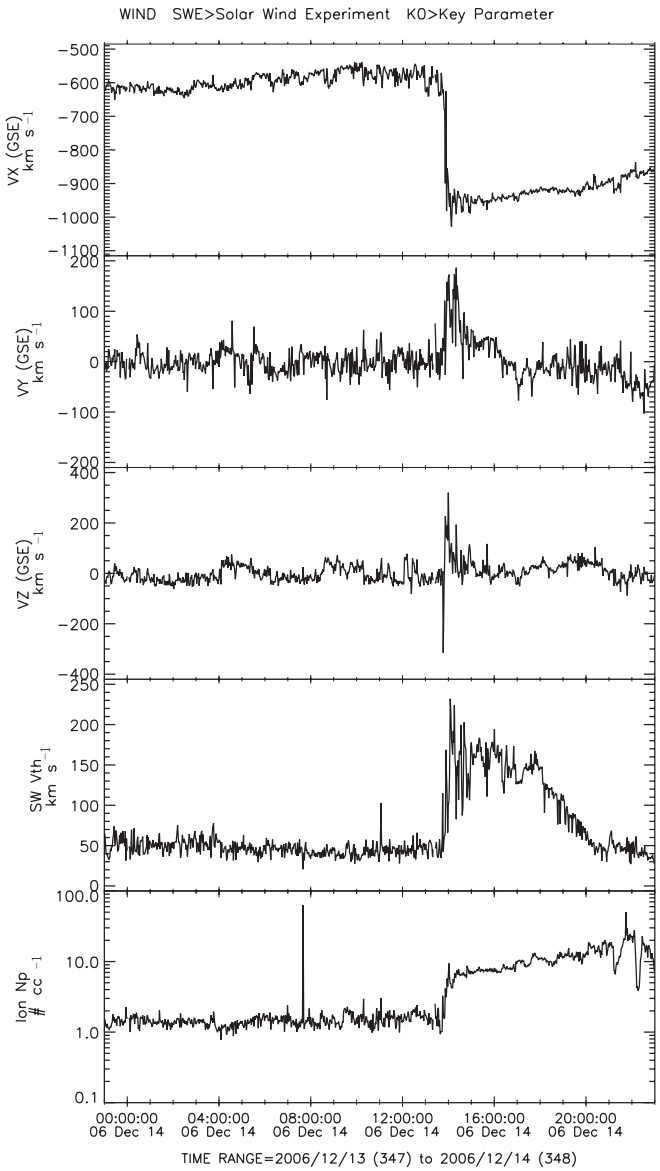

Fig. 1 The plot shows the key parameters of the 2006 December 14 shock event observed by the Wind spacecraft. The data come from *http://cdaweb.gsfc.nasa.gov/cdaweb*.

higher energy range, as expected from velocity dispersion. There was also a higher background in the lower energy range associated with the 13 December solar event and the related shock (von Rosenvinge et al. 2009). Simultaneously, many spikes were also detected that were superposed on the radio continuum in the frequency range 2.6–3.8 GHz recorded by digital spectrometers of National Astronomical Observatories, Chinese Academy of Sciences (NAOC). These spikes were found to have complex structures associated with other radio burst signatures connected with observations of the in-situ SEP event (Wang et al. 2008).

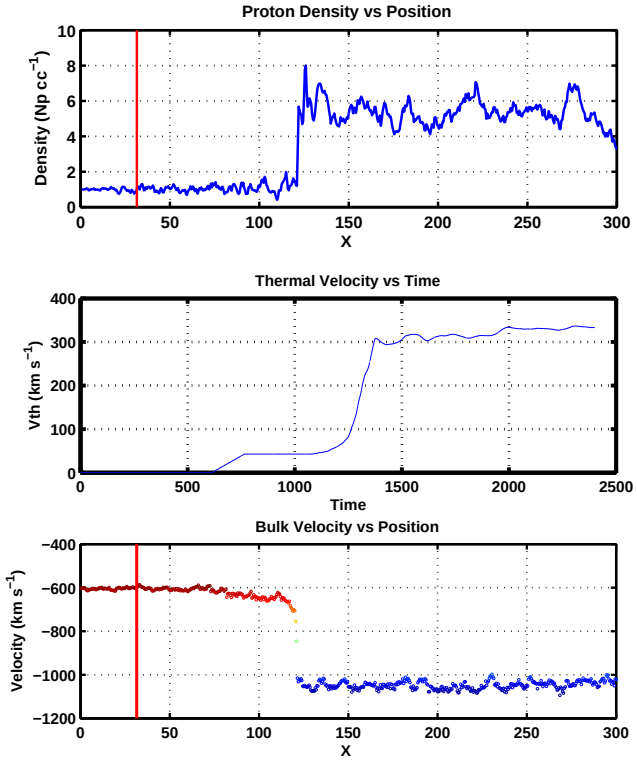

Fig. 2 The upper panel represents the proton density profile vs its position at the end of the simulation. The middle panel denotes the solar wind's thermal velocity profile in the local frame vs time. The lower panel indicates the speed of the bulk flow profile vs its position at the end of the simulation. The vertical lines in the upper and lower panels both show the final position of the free escape boundary at the end of the simulation.

Both Wind and ACE were in orbit around the $L1$ Lagrangian point about 1.5 million km upstream of the Earth. Similar intensity modulations were observed by Wind and ACE. As has also been noted by Mulligan et al. (2008), the variations in the particle intensity and smooth magnetic fields observed by near-Earth spacecraft occurred during the interplanetary coronal mass ejection (ICME) driving the shock on 14 December which was related to the 13 December solar event. Solar wind observations from ACE show evidence of the presence of the ICME, which had an enhanced magnetic field and a smooth rotated "magnetic cloud" in the upstream shock and the intervening sheath region, respectively. According to the magnetic cloud list compiled by Wind, the axis orientation of this "magnetic cloud" was $\theta = 27°$, $\phi = 85°$. In addition, Liu et al. (2008) estimated that the direction of "cloud's" axis was $\theta = -57°$, $\phi = 81°$ in Geocentric Solar Ecliptic (GSE) coordinates. Thus, both agree that the axis was closely aligned west to east but differ about whether it was inclined north or south, most likely because different intervals were considered in their analyses.

Figure 2 shows a group of profiles of the physical parameters in the simulation. From top to bottom, the upper panel shows the proton density profile vs its position. The proton density is represented by the scaled value. The enhanced density flux apparently appears in the position of the shock front. The density in the downstream region is about five times higher than in the upstream bulk flow that was not affected by the shock. By comparing the proton density profiles between

Table 1 The Parameters of the Simulated Shock

Simulated Parameter		Dimensionless value	Scaled value
Physical	Upstream bulk speed	$U_{\rm u} = -0.4467$	-600 km s^{-1}
	Downstream bulk speed	$U_{\rm d} = -0.7742$	-1042 km s^{-1}
	Relative inflow velocity	$\Delta U = 0.3275$	442 km s^{-1}
	Inflow sonic Mach number	$\rm M = 17.5$	...
	Thermal speed	$v_0 = 0.0342$	46 km s^{-1}
	Scattering time	$\tau = 0.3333$	0.052 s
Numerical	Box size	$X_{\rm max} = 300$	$10R_{\rm e}$
	Total time	$t_{\rm max} = 2400$	6.3 min
	Time step size	$dt = 1/30$	0.0053 s
	Number of zones	$n_x = 600$	...
	Initial particles per cell	$n_0 = 650$	...
	FEB distance	$X_{\rm feb} = 90$	$3R_{\rm e}$

Notes: The physical parameters are taken from the Wind spacecraft, and the numerical parameters are derived from the 2006 December 14 CME-driven shock.

Figures 2 and 1, the simulated downstream bulk flow has a slightly higher proton density than in the observed downstream bulk flow. The middle panel in Figure 2 denotes that the thermal velocity profile evolves with time. The profile at time $t \sim 600$ (it is zero before time $t < 600$ in the simulation, taking account of the injection from the pre-inflow box) initially has a Maxwellian thermal velocity of $v_0 = 46$ km s^{-1} until it is shocked. After the profile is shocked, as shown in the middle panel of Figure 2, it reaches an average thermal velocity of around $\langle v_{\rm d} \rangle = 300$ km s^{-1} till the end of the simulation. Also the thermal velocity profile shows a slightly larger enhancement than that from the observation by the Wind spacecraft. Although the simulated proton density and the thermal velocity of the solar wind are slightly larger than those from in-situ observations, we suggest that this is caused by an insufficient number of particles in the simulation. We have demonstrated this using a series of simulations with different initial numbers of particles per cell. The lower panel indicates the profiles of the bulk flow speed vs its position at the end of the simulation. The profile shows an upstream bulk flow speed $U_{\rm u} = -600$ km s^{-1} and a downstream bulk flow speed $U_{\rm d} = -1042$ km s^{-1} which are consistent with the observations.

3 THE METHOD

3.1 Physical Model

We consider a plane-parallel shock where the supersonic flow moves from the Sun to the Earth (in the rest frame) along the x-axis direction. The shock was observed by the Wind, SOHO, and ACE spacecraft near the Earth at the location of the first Lagrangian point $L1 \sim 1.5$ million km ($\sim 250R_{\rm e}$, where $R_{\rm e}$ is the radius of the Earth) upstream of the Earth on 14 December. All trajectories of the spacecraft on the 348th day corresponding to 2006 December 14 are shown in Figure 3. With the CME-driven shock propagating from the Sun along the *x*-axis to the Earth, its shock front was encountered by Wind, SOHO, and ACE spacecraft located in $X_{\rm GSE}$ between the $250R_{\rm e}$ and $180R_{\rm e}$ upstream from the Earth. These three spacecraft moved about $10R_{\rm e}$ in their orbits on the 348th day. The distances of all these spacecraft from the Sun-Earth line were within $50R_{\rm e}$ along the $Y_{\rm GSE}$ and $Z_{\rm GSE}$ directions. The 2006 December 14 shock event originated from the western hemisphere of the Sun with an interplanetary "magnetic cloud" axis orientation of $\theta = 27^\circ$, $\phi = 85^\circ$. The actual trajectory of the Wind spacecraft at that moment was just tangent to the Sun-Earth line at an angle $\phi = 80^\circ$ as shown in the lower panel of Figure 3. From the perspective of the Wind spacecraft, the observed CME-driven shock is just a parallel diffusive shock, so its observations provided an

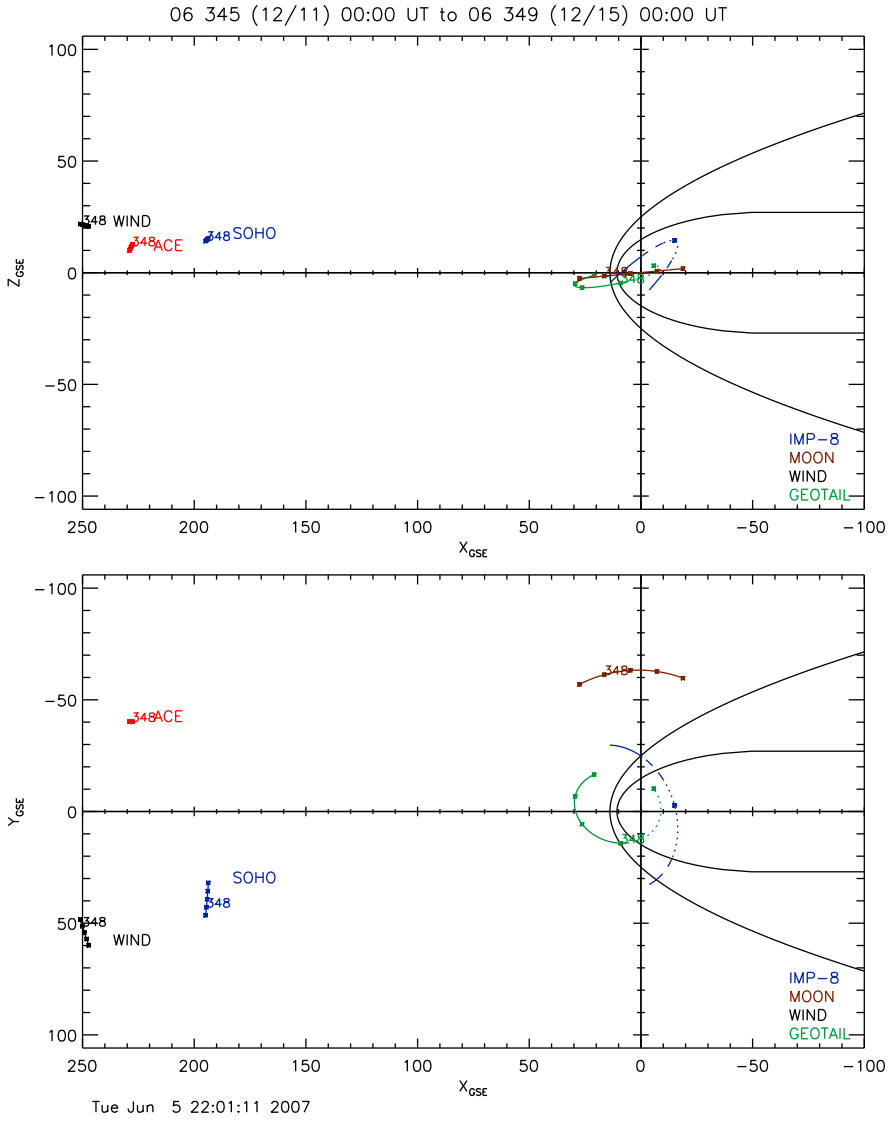

Fig. 3 The diagrams show the orbits of the near-Earth spacecraft. The orbital data are taken from *http://cdaweb.gsfc.nasa.gov/cdaweb*.

example of a semi-parallel shock. In this case, we can apply our dynamical Monte Carlo code to understand the particle injection problem of DSA theory.

The important physical parameters of this simulation include the upstream bulk flow velocity ($U_{\rm u}$), the downstream bulk flow velocity ($U_{\rm d}$), the relative difference in bulk inflow velocity (ΔU), the inflow sonic Mach number ($|U_{\rm d}|/c_{\rm s}$), which is 17.5 (where $c_{\rm s} \equiv (\gamma kT/m)^{1/2}$, $c_{\rm s}$ is the upstream sound speed), the upstream thermal velocity [$v_0 \equiv (kT/m)^{1/2}$], and the constant scattering time (τ), which is 2/5 times the scattering time ($\tau_0 = 0.13\,{\rm s}$) used by Knerr et al. (1996) in the simulation of Earth's bow shock. Since there are some differences in the shock geometry between the CME-driven shock (i.e. at the $L1$ point) and the Earth-bow shock, we chose the scattering time 0.4 times smaller

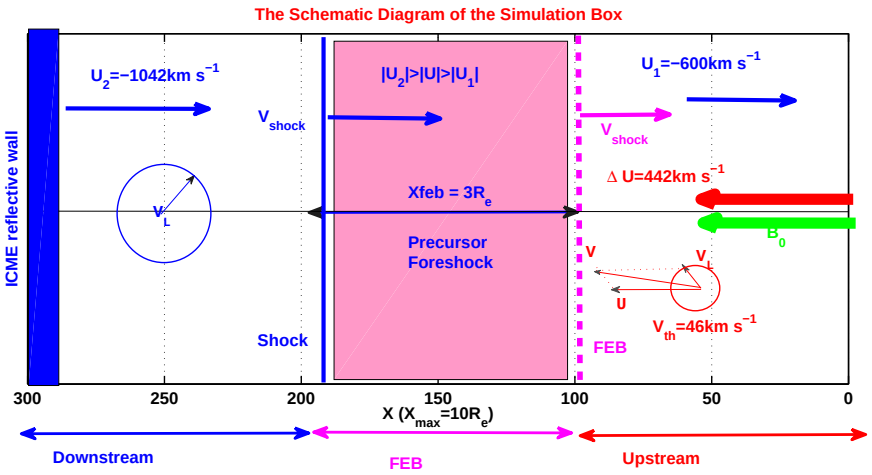

Fig. 4 A schematic diagram of the simulation box. The left reflective wall produces the ICME-driven shock that propagates from the left boundary to the right boundary.

than that in the bow shock of Earth, which is equivalent to a 2.5 times larger free escape boundary (FEB) distance than that in the Earth-bow shock. The specific physical parameters and numerical parameters are listed in Table 1 with their dimensionless values and scaled values, respectively.

3.2 Mathematical Model

According to the observed 2006 December 14 CME-driven shock, the simulation box can be designed as a one-dimensional parallel shock along the direction of the x-axis. As shown in Figure 4, the initial particles with a difference in relative bulk flow speed (ΔU) move from right to left. The particles initially have a Maxwellian thermal distribution with an initial temperature ($T_0 \equiv mv_0^2/k$) in the local frame. To begin and maintain the shock simulation, particles are assumed to flow into the simulation box from the pre-inflow box at the right boundary. Then, with the continuous flow of particles moving forward one time step, only those particles which move into the main simulation box are actually added to the simulation. This process naturally leads to a population of inflowing particles that is weighted by flux. At the left boundary of the box, a reflective wall acts to produce a CME-driven shock moving from left to right. Considering the geometry of the shock event from the 14 December shock, we just follow the parallel component of the CME-driven shock observed by the Wind spacecraft.

Figure 4 also shows one typical particle and its local ($V_{\rm L}$) or box frame (V) velocity in the upstream region and downstream region. The majority of the incoming particles cross the shock front only once from the upstream region to the downstream region and stay in the downstream region. A small portion of the particles can effectively scatter off the resonant magnetohydrodynamic (MHD) wave self-generated by the energetic particles and return to the upstream region to re-cross the shock front for additional energy gains (Liu et al. 2004). Thus an anisotropic energetic particle distribution, but not a strict Maxwellian distribution, is produced in the diffusive regions. It is this elastic interaction between individual particles and the collective background that allows the Fermi acceleration to occur.

The position of the FEB could coincide with a location upstream of the shock where particles are no longer able to scatter effectively and return to the shock. A reasonable FEB farther out in front of the shock moves, accompanying the shock front, at the same shock evolutional velocity $V_{\rm sh}$. As shown by the shaded area in the middle of Figure 4, the constant FEB distance maintains a precursor region in front of the shock for the particle acceleration. If one particle archives the highest energy, and exceeds the position of the FEB in front of the shock, it will be regarded as an escaped particle and removed from the simulation system. According to the actual motion of the Wind spacecraft over the duration, the spacecraft moved a distance of about $10R_{\rm e}$ in their orbits on the 348th day. To simulate the shock's formation and evolution, the total length of the simulation box is set to be $10R_{\rm e}$, and the length of the FEB is set to be $\sim 3R_{\rm e}$. The scattering time is set to be $\tau = 0.052$ s based on the bow shock model of Earth (Knerr et al. 1996).

The important numerical parameters include the box size ($x_{\rm max}$), the time to evolve the whole system ($t_{\rm max}$), the number of grid zones (n_x), the initial number of particles per zone (n_0), and the size of the time step (dt). Because of the similarity with the plasma flow near Earth, we take some numerical parameters from Earth's bow shock model (Knerr et al. 1996). Specifically, the total box length $x_{\rm max} = 300$ is divided into $n_x = 600$ grids, with each grid length being $\Delta x = 1/2$; the total time $t_{\rm max} = 2400$ is divided into $n_t = 72\,000$ steps by dt, with each step being $dt = 1/30$. All numerical parameters are listed in Table 1. The physical and numerical parameters constitute the whole list of parameters used in the simulation. As shown in Table 1, each dimensionless value corresponds to its scaled value. The scale factors for distance, velocity, and time are $x_{\rm scale} = 10R_{\rm e}/300$, $v_{\rm scale} = 442\,{\rm km\ s^{-1}}/0.3275$, and $t_{\rm scale} = x_{\rm scale}/v_{\rm scale}$, respectively.

The simulations apply the same steps as the bow shock model of the Earth (Knerr et al. 1996) including three sub steps: (i) All the particles move with their velocities in the simulation box along the direction of the x-axis. (ii) Summations of particle masses and velocities are performed over each computational grid. (iii) The scattering angular distribution law is invoked. The processes of particle diffusion in the presented simulations are dominated by a Gaussian angular scattering distribution. The scattering rate is $R_{\rm s} = dt/\tau$, which implies that only this fraction of particles is able to scatter off the scattering center which is fixed in the background fluid. The candidate does not change its route until it is selected to scatter once again, so the particle's mean free path is proportional to the thermal velocities in the local frame with

$$\lambda = V_{\rm L} \cdot \tau\,. \tag{1}$$

For an individual proton, the grid-based scattering center can be seen as a sum of individual momenta, so these scattering processes can be taken as elastic collisions. In an increment of time, once all of the candidates complete these elastic collisions, the momentum of the grid-based scattering center is changed. In turn, the momentum of the grid-based scattering center will affect the momenta of the individual particles in their corresponding grid at the next increment of time. One complete time step consists of the above three substeps. The total simulation temporally evolves forward by repeating this time step sequence. To calculate the scattering processes accurately and produce a mean free path following an exponential distribution, the time step should be less than the scattering time (i.e. $dt < \tau$).

The scattering angles consist of two variables: $\delta\theta$ and $\delta\phi$. Once a particle has a collision with the background scattering centers, its pitch angle becomes $\theta' = \theta + \delta\theta$, and the azimuthal angle becomes $\phi' = \phi + \delta\phi$, where $\delta\theta$ is the variation in the pitch angle θ and $\delta\phi$ is the variation in the azimuthal angle ϕ. The pitch angles θ and θ' are both in the range $0 \leq \theta$, $\theta' \leq \pi$, and azimuthal angles ϕ and ϕ' are both in the range $0 \leq \phi$, $\phi' \leq 2\pi$ on the unit sphere. The variations in the pitch angle $\delta\theta$ and azimuthal angle $\delta\phi$ are composed of the scattering angle, and its anisotropy is described by the Gaussian function $f(\delta\theta, \delta\phi)$. Here, we will just present the results of the CME-driven shock using the Gaussian distribution of scattering angles with a standard deviation value of $\sigma = \pi$.

4 RESULTS

4.1 Data Analysis

Since an individual particle's energy can be examined at any given time during the simulation, the energy function over time can be obtained. At first, we can calculate the necessary energy functions for further analysis. In this simulation, we obtained the total energy function in the box, the energy loss function that describes escaping from the FEB, and the injected energy function which is the summation of energy of the injected energetic particles from the downstream region at the local velocity of $V_{\rm L} = U_0$ over time. Then, at the end of the simulation, we obtained the final values of the total energy $E_{\rm tot} = 3.5666$, the energy loss $E_{\rm loss} = 0.2010$, and the energy injection $E_{\rm inj} = 0.5464$. The final energy injection rate $R_{\rm inj}$, which represents the efficiency of acceleration, can be defined by the formula

$$R_{\rm inj} = E_{\rm inj}/E_{\rm tot}\,. \tag{2}$$

The injection rate is very important for a CME-driven shock, because it is connected with the process of how the shock distributes energy to accelerate cosmic ray (CR) particles and "heat" the thermal background plasma. By a series of simulations, we give a plausible injection rate with a value of $R_{\rm inj} = 15.32\%$ for the 2006 December 14 shock. Under this condition, we obtain the maximum energy of a particle with the dimensionless value of $VL_{\rm max} = 20.2609$ and the scaled value of $E_{\rm max} = 3.8684$ MeV. In addition, because there exist some energy losses in the simulated system, fine structures in the shock do not completely agree with the situ observations. Finally, according to DSA theory, the energy spectral index can be calculated based on the simulated compression ratio (i.e., $\Gamma = (r+2)/[2(r-1)]$). We calculated the total energy spectral index with a value of $\Gamma_{\rm tot} = 0.8406$ and the vortex subshock energy spectral index with a value of $\Gamma_{\rm sub} = 1.1074$.

Figure 5 shows the simulated energy spectra. The top plot shows the energy spectrum with the "double-peak" structures averaged over the entire simulated box at the end of the simulation. The bottom plot shows an energy spectrum with a "power-law" tail averaged only over the downstream region at the end of the simulation. In this plot, the thick solid curve with a narrow peak represents the initial Maxwellian thermal energy spectrum in the shock frame. As viewed from the top plot, the double peaks imply that there exist two thermal particle distributions in the entire simulated box: the left peak represents the distribution of the "heated" downstream flow and the right peak represents the Maxwellian distribution of the unshocked upstream flow. Looking at the bottom plot, we find the final extended energy spectrum in the left side of the panel appears several tens of times wider than that in the initial energy spectrum in the right side of the panel. This means that there exists a large temperature difference between the shocked downstream region and the unshocked upstream region.

As shown in Figure 6, the spectra recorded by ACE, STEREO, and SAMPEX instruments observing protons in the two largest SEP events that occurred December 2006 are reported. The particle intensities started increasing at the beginning of the 5 December event and also at the onset of the 13 December event. These two events both have spectra that roll over in a similar fashion beyond $\sim$50 MeV, as in the SEP event that occurred 2005 January 20 (Mewaldt et al. 2008; Wang et al. 2009; Bartoli et al. 2012; Wang et al. 2010). The fitted shape of the spectral energy distribution of the 2006 December 12–14 events are shown in the right panel and the spectral index is marked as a value of $E^{-1.07}$ in the lower energy range. The predicted subshock energy spectral index ($\Gamma_{\rm sub} = 1.1074$) from our simulation is consistent with the observed energy spectral index in the lower energy range. Owing to computational constraints on the size of the simulation grid, this simulated energy spectrum is only in the range from keV to MeV. We speculate that the second "roll over" on the higher energy spectrum could be obtained if a larger simulation box size were used. This will be investigated in a future simulation. There are two conditions suggesting that the "roll-over" would be reproduced at high energy:

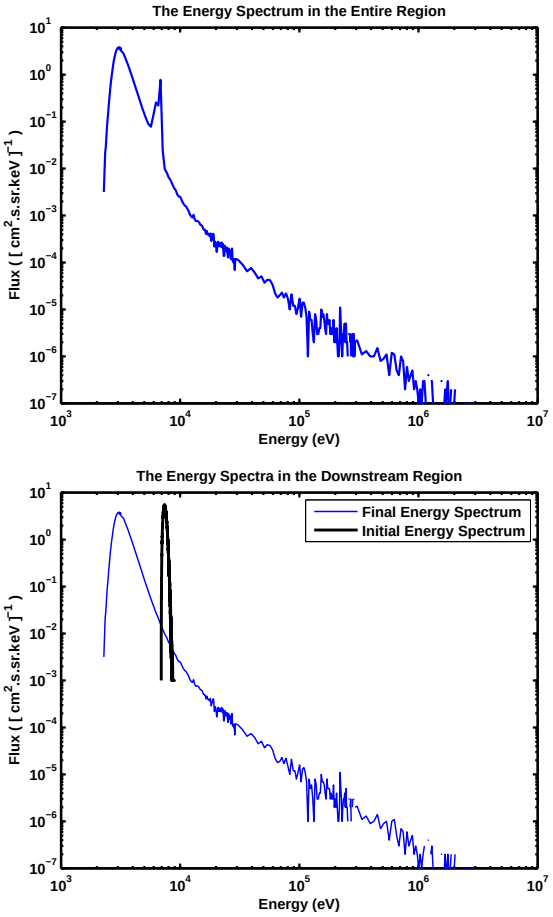

Fig. 5 The extended energy spectra in the two plots are calculated over the entire simulation region (*top)* and only the downstream region at the end of the simulation (*bottom)*. The solid extended curve with a "power-law" tail in each plot represents the final shocked energy spectrum. The thick curve with a narrow peak denotes the initial Maxwellian energy spectrum.

(1) The FEB distance controls the maximum diffusive length (i.e. $\mathrm{FEB} \equiv \lambda_{\max} = \tau \cdot p_{\max}$). If we enlarge the FEB distance and the size of the simulation box, we could obtain a larger $P_{\max}$ in the new simulated system.
(2) In Figure 6, we can see the first power law $E^{-1.07}$ as the input function of the second power law $E^{-2.45}$ at the high energy range. Moreover, in Figure 5, we can see the heated Maxwellian thermal distribution, which would be represented by a similar power law $E^{-0.5}$ averaged over the respective energy range, as the input function of the first power law $E^{-1.1074}$.

4.2 Shock Structures

At the end of the simulation, the derived parameter values are given as follows: the shock position $X_{\rm sh} = 121.5$, the FEB position $X_{\rm f} = 31.5$, the shock's evolutional velocity $V_{\rm sh} = -0.0744$, the subshock velocity $V_{\rm sub} = 0.2103$, total compression ratio $r_{\rm tot} = 5.4034$, subshock's compression

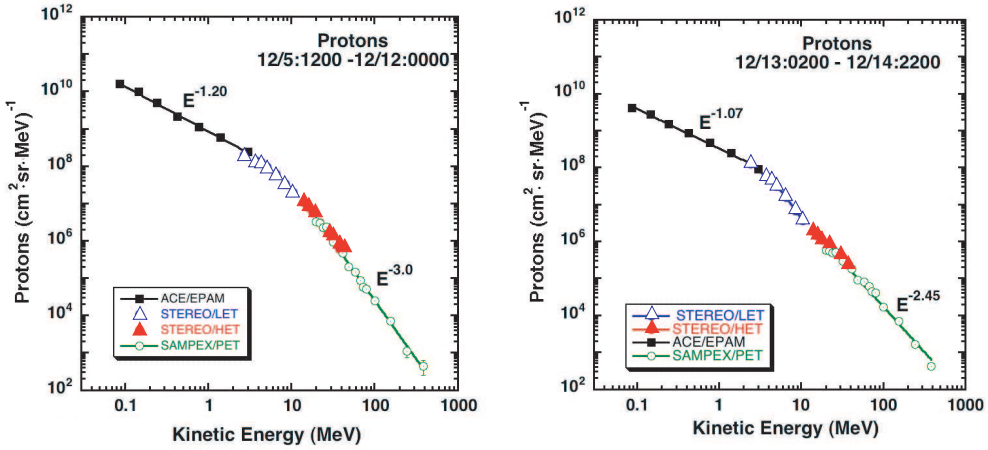

Fig. 6 Fluency spectra of the protons in the two largest SEP events that occurred in December 2006 measured by multiple spacecraft. The energy range is from 5 to 100 MeV, adopted from Mewaldt et al. (2008).

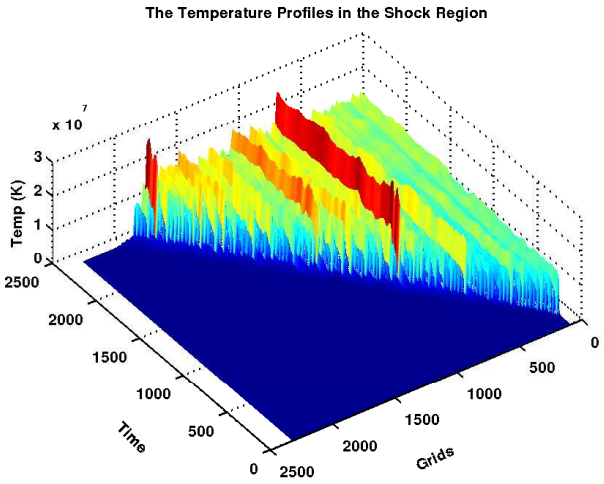

Fig. 7 The mesh plot represents temperature profiles of the evolutional bulk flow in terms of their positions over time. The lower temperature represents the upstream bulk flow. The higher temperature represents the downstream bulk flow. The obvious boundary traces the positions of the shock front with time.

ratio $r_{\rm sub} = 3.4697$, total energy spectral index $\Gamma_{\rm tot} = 0.8406$, energy spectral index of the subshock $\Gamma_{\rm sub} = 1.1074$, particle injection rate $R_{\rm inj} = 15.32\%$, energy loss $E_{\rm loss} = 0.2010$, the local velocity of the particle with maximum energy $VL_{\rm max} = 20.2609$, and the maximum energy of the particles $E_{\rm max} = 3.8684\,$MeV.

We present the evolution of the entire shock with the temperature profile of the time sequences as shown in Figure 7. The supersonic continuous inflow with an initial Maxwellian thermal velocity v_0

in each grid evolves from the beginning to the end of the simulation. Their kinetic energies are translated into random thermally-energetic particles by the "heating" processes in the downstream region resulting in a distinct enhancement of the temperature profiles in the shock front with time. The profile of thermal temperature shows the averaged upstream temperature of $T_0 = 2.5 \times 10^5$ K and the averaged downstream temperature of $T_{\rm d} = 9.0 \times 10^6$ K. This means that the CME-driven shock can "heat" the background plasma efficiently and provide the first-order Fermi acceleration mechanism by crossing the shock front to accelerate the particles, which are injected from the "heated" downstream region into the precursor region.

The complex fine structure of the shock front at the end of the simulation is shown in Figure 8. The final evolutional positions of the FEB and the shock front are $X_{\rm f} = 31.5$ and $X_{\rm sh} = 121.5$ on the x-axis, respectively. The distance between these two locations is just the size of the precursor region where the particle acceleration processes occur. The incoming upstream bulk flow speed $U_{\rm u}$ is slowed by this precursor region down to the downstream bulk flow speed $U_{\rm d}$ in this region. The bulk flow speed in the precursor region is between the two bulk flow speeds (i.e. $U_{\rm u} > U_{\rm p} > U_{\rm d}$). From our simulation, we can see that the particle acceleration process and the "back pressure" due to the energetic particles occurred mostly in the precursor region, which results in a non-linear shock structure that is characterized by a gradient in the bulk flow speed. According to the evolutional shock front position $X_{\rm sh}$ as a function of time, we can calculate the shock's evolutional velocity $V_{\rm sh}$ as

$$V_{\rm sh} = \frac{|X_{\rm max} - X_{\rm sh}|}{t_{\rm max}}\,, \tag{3}$$

where $X_{\rm max}$ is the total length of the simulation box, and $t_{\rm max}$ is the total simulation time. Then, we are able to calculate the total shock compression ratio in the shock frame as

$$r_{\rm tot} = \frac{\Delta U + |V_{\rm sh}|}{|V_{\rm sh}|}\,, \tag{4}$$

where ΔU is the relative bulk flow speed between the upstream and downstream, and $V_{\rm sh}$ is the shock velocity.

Figure 8 shows the shock's fine structure with the bulk flow speed near the shock front at the end of the simulation. $V_{\rm sub} = 0.2103$ shows the bulk flow speed of the subshock, $V_{\rm d} \simeq 0$ shows the bulk flow speed of the downstream region, $V_{\rm sh} = -0.0744$ represents the value of the shock's evolutional velocity in the opposite direction, and $U_0 = 0.3275$ represents the incoming bulk flow speed with a difference in the related bulk flow speed of ΔU. All zones of the precursor, subshock and downstream are divided by a vertical dashed line and a solid line in the plot. These three zones constitute the fine structure of the total shock in the region of the simulated shock. The smooth precursor has a long scale in the range from the subshock's position $X_{\rm sub}$ to the FEB position $X_{\rm f}$, which is invisible, beyond the left boundary of the plot. This zone is called the diffusive zone where the bulk flow speed will be slowed by the "back pressure" of the accelerated particles. The subshock region with a narrow scale of three grid spacings has a deep drop of the bulk flow speed, in which the bulk flow speed varies from the subshock velocity $V_{\rm sub}$ to the downstream velocity $V_{\rm d}$. The scale of the three-grid-length is almost identical to the averaged thermal mean free path over the downstream region. The subshock velocity $V_{\rm sub}$ is determined by the horizontal dot-dashed line with a value of $V_{\rm sub} = 0.2103$. The downstream velocity $V_{\rm d}$ at the end of the simulation is marked with a horizontal dashed line, which should have an averaged value of $\langle V_{\rm d}\rangle = 0$ over the entire simulation time in the box frame. The evolutional velocity of the negative shock evolution marked with a horizontal solid line shows a value of $V_{\rm sh} = -0.0744$. We can calculate the subshock's compression ratio according to Rankine-Hugoniot relationships in the shock frame as

$$r_{\rm sub} = \frac{V_{\rm sub} + V_{\rm sh}}{\langle V_{\rm d}\rangle + V_{\rm sh}}\,, \tag{5}$$

where we take the averaged value of the downstream velocity $\langle V_{\rm d}\rangle$ equal to zero.

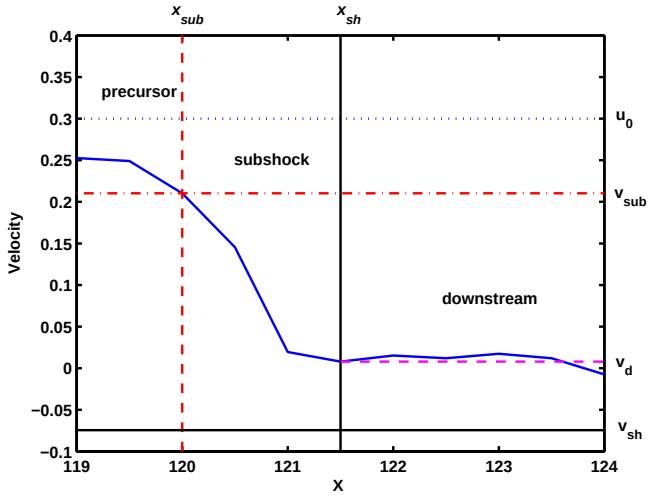

Fig. 8 The fine structure of the bulk flow speed at the end of the simulation. The vertical dashed line and vertical solid line split the entire region into three sections: precursor, subshock and downstream regions.

5 SUMMARY AND CONCLUSIONS

In summary, we performed dynamical Monte Carlo simulations on the 2006 December 14 shock driven by a CME using an anisotropic scattering law. The specific temperature profile, shock fine structures, and particle injection function, as functions of time, were presented. We examined the correlation between the processes of energy injection and shock energy translation in the interplanetary CME-driven shock. In addition, we found the simulated energy spectrum from the CME-driven shock provides a good fit to the observations from multiple spacecraft.

In conclusion, the dynamical Monte Carlo simulation of the CME-driven shock that occurred on 2006 December 14 demonstrates that the energy spectrum is affected by the specific non-linearity of the DSA. This paper focuses on the energy injection, which is one of the important nonlinear effects of the DSA. By calculating the energy injection rate of the CME-driven shock, we can understand how the CME-driven shock distributes its shock energy to accelerate the energetic particles by the mechanism of first-order Fermi acceleration as well as how it heats the background bulk flow of the solar wind at a certain efficiency. We give an energy injection rate of $R_{\rm inj} = 15.32\%$ in the 2006 December 14 CME-driven shock. We suggest that this predicted injection rate could satisfy the required energies of the observed SEP events, which should be released from the CME-driven shock.

Acknowledgements The work was supported by the National Natural Science Foundation of China (Grant No. 10921303), and the National Basic Research Program of the Ministry of Science and Technology (MOST Grant No. 2011CB 811401).

References

Axford, W. I., Leer, E., & Skadron, G. 1977, in Proc. 15th International Cosmic Ray Conference (Plovdiv), 11, 132

Bartoli, B., Bernardini, P., Bi, X. J., et al. 2012, ApJ, 745, L22

Bednarz, J., & Ostrowski, M. 1999, MNRAS, 310, L11

Bell, A. R. 1978, MNRAS, 182, 147
Berezhko, E. G., & Völk, H. J. 2000, A&A, 357, 283
Blandford, R. D., & Ostriker, J. P. 1978, ApJ, 221, L29
Bykov, A. M., & Treumann, R. A. 2011, A&A Rev., 19, 42
Bykov, A. M., Uvarov, Y. A., Bloemen, J. B. G. M., et al. 2009, MNRAS, 399, 1119
Cane, H. V., Reames, D. V., & von Rosenvinge, T. T. 1991, ApJ, 373, 675
Caprioli, D., Amato, E., & Blasi, P. 2010, Astroparticle Physics, 33, 307
Drury, L. O., Axford, W. I., & Summers, D. 1982, MNRAS, 198, 833
Drury, L. O., & Voelk, J. H. 1981, ApJ, 248, 344
Ellison, D. C., & Eichler, D. 1984, ApJ, 286, 691
Ellison, D. C., Moebius, E., & Paschmann, G. 1990, ApJ, 352, 376
Hu, H. 2009, arXiv:0911.3034
Kang, H., & Jones, T. W. 2007, Astroparticle Physics, 28, 232
Knerr, J. M., Jokipii, J. R., & Ellison, D. C. 1996, ApJ, 458, 641
Krymskii, G. F. 1977, Akademiia Nauk SSSR Doklady, 234, 1306
Le, G., Cai, Z., Wang, H., & Zhu, Y. 2012, Ap&SS, 339, 151
Li, C., Dai, Y., Vial, J.-C., et al. 2009, A&A, 503, 1013
Liu, S., Petrosian, V., & Mason, G. M. 2004, ApJ, 613, L81
Liu, Y., Luhmann, J. G., Müller-Mellin, R., et al. 2008, ApJ, 689, 563
Lu, Q. M., Xia, L. D., & Wang, S. 2006, Journal of Geophysical Research (Space Physics), 111, A09101
Malkov, M. A., Diamond, P. H., & Völk, H. J. 2000, ApJ, 533, L171
Malkov, M. A., & O'C Drury, L. 2001, Reports on Progress in Physics, 64, 429
Mewaldt, R. A., Cohen, C. M. S., Cummings, A. C., & et al. 2008, in Proceedings of the 30th International Cosmic Ray Conference (Mexico), 1, 107
Miller, J. A. 1997, ApJ, 491, 939
Mulligan, T., Blake, J. B., & Mewaldt, R. A. 2008, in International Cosmic Ray Conference (Mexico), 1, 179
Pick, M., & Vilmer, N. 2008, A&A Rev., 16, 1
Qin, G., & Shalchi, A. 2009, ApJ, 707, 61
Verkhoglyadova, O. P., Li, G., Zank, G. P., et al. 2010, Journal of Geophysical Research (Space Physics), 115, A12103
Vladimirov, A., Ellison, D. C., & Bykov, A. 2006, ApJ, 652, 1246
von Rosenvinge, T. T., Richardson, I. G., Reames, D. V., et al. 2009, Sol. Phys., 256, 443
Wang, B., Yuan, Q., Fan, C., et al. 2010, Science in China G: Physics and Astronomy, 53, 842
Wang, J., Shi, Z., Wang, H., & Lue, Y. 1996, ApJ, 456, 861
Wang, J., Zhao, M., & Zhou, G. 2009, ApJ, 690, 862
Wang, S. J., Yan, Y. H., Liu, Y. Y., et al. 2008, Sol. Phys., 253, 133
Wang, X., & Yan, Y. 2011b, arXiv:1111.0162
Wang, X., & Yan, Y. H. 2011a, A&A, 530, A92
Yan, Y., Pick, M., Wang, M., Krucker, S., & Vourlidas, A. 2006, Sol. Phys., 239, 277
Zhang, J., Dere, K. P., Howard, R. A., Kundu, M. R., & White, S. M. 2001, ApJ, 559, 452
Zhang, J., Solanki, S. K., Woch, J., & Wang, J. 2007, A&A, 471, 1035
Zhang, J.-L., Bi, X.-J., & Hu, H.-B. 2006, A&A, 449, 641
Zirakashvili, V. N. 2007, A&A, 466, 1